Sources of Quasi-Periodic Pulses in the 18 August 2012 Flare

Solar Physics

A. Altyntsev¹ · N. Meshalkina¹ · H. Mészárosová² · M. Karlický² · V. Palshin³ · S. Lesovoi¹ ·

© Springer ••••

Abstract We analyzed spatial and spectral characteristics of quasi-periodic pulses (QPP) for the 18 August 2012 limb flare, using new data from a complex of spectral and imaging instruments developed by the Siberian Solar Radio Telescope team and the Wind/Konus gamma-ray spectrometer. A sequence of broadband pulses with periods of approximately ten seconds were observed in Xrays at energies between 25 keV and 300 keV, and in microwaves at frequencies from a few GHz up to 34 GHz during an interval of one minute. The QPP Xray source was located slightly above the limb where the south legs of large and small EUV loop systems were close to each other. Before the QPPs the soft X-ray emission and the Ramaty High Energy Solar Spectroscopic Imager signal from the energy channels below 25 keV were gradually arising for several minutes at the same location. It was found that each X-ray pulse showed the soft-hard-soft behavior. The 17 and 34 GHz microwave source were at footpoints of the small loop system and the source emitting in the 4.2-7.4 GHz band in the large one. The QPPs were probably generated by modulation of acceleration processes in the energy release site. Analyzing radio spectra we determined the plasma parameters in the radio sources. The microwave pulses could be explained by relatively weak variations of the spectrum hardness of emitting electrons.

Keywords: Radio Emission, Active Regions; Oscillations, Solar; X-Ray Bursts, Association with Flares

¹ Institute of Solar-Terrestrial Physics SB RAS, Lermontov st. 126A, Irkutsk 664033, Russian Federation email: altyntsev@iszf.irk.ru email: nata@iszf.irk.ru email: svlesovoi@gmail.com

² Astronomical Institute of the Academy of Sciences of the Czech Republic, CZ–25165 Ondřejov, Czech Republic email: hana.meszarosova@asu.cas.cz email: marian.karlicky@asu.cas.cz

³ Ioffe Physical Technical Institute, St. Petersburg, 194021, Russian Federation email: val@mail.ioffe.ru

1. Introduction

Solar flares are known to produce large quantities of accelerated electrons. However, the location and physical properties of the acceleration region of high-energy electrons are not well understood. Hence, determination of properties of an acceleration region from spatially resolved observations of flare emission is under active study. In particular, the study of events with a quasi-periodic behavior of hard X-rays and microwaves (MW) on time scales of several seconds is important. The periodicity behaviors in X-ray/MW may reveal the characteristic time scales of processes in the source region.

The nature of quasi periodical pulses (QPP) is under debate; nevertheless, two basic mechanisms for fluctuating QPP have been proposed. One mechanism relates the phenomenon to changes of plasma parameters in microwave sources due to MHD oscillations in flare loops. Usually, sausage, kink, torsion, and slow sound modes are considered (e.g. Roberts, Edwin, and Benz, 1984; Nakariakov and Melnikov, 2009). In this approach the X-ray oscillations appear due to variations of particle precipitation, which can be caused by a modulation of a pitch angle and a mirror ratio in the loop footpoints. In microwaves, we can observe MHD modulations of the source parameters such as magnetic field, plasma density, temperature, electron distribution function, and the source dimensions (e.g. Aschwanden, 1987; Grechnev, White, and Kundu, 2003). A quantitative study of the observable MW signatures of the MHD oscillation modes in the coronal loops was performed by Mossessian and Fleishman (2012). On the other hand the efficiency of particle acceleration mechanisms may strongly depend on changes of plasma parameters in acceleration sites, and the X-ray and microwave emission can therefore clearly respond to relatively weak disturbances associated with the MHD ones (e.g. Asai et al., 2001; Kallunki and Pohjolainen, 2012). In all of these cases we can expect that the QPP periods will be close to the periods of the MHD oscillations or their harmonics (Nakariakov et al., 2006). The main problem is the lack of identification of the oscillation mode because, as a rule, available observations do not determine plasma and geometric properties of the oscillation loops.

In the second mechanism, QPP is considered to be caused by some intrinsic property of primary energy release (Nakariakov and Melnikov, 2009). Models with an electron-acceleration modulation naturally explain the simultaneity of the oscillations in different emission bands. Moreover, the high modulation of QPP can be easily achieved, because it is controlled by the variations of nonthermal electron density. The current-loop coalescence instability proposed by Tajima, Brunel, and Sakai (1982) and Tajima et al. (1987) belongs to this category. They have studied the current-loop coalescence instability by numerical simulation and showed that the stored magnetic energy can be explosively converted into particle kinetic energy. They also showed that the current loop coalescence instability can produce the QPPs with a period about the Alfvén transit time "across" the current-loop. However, the theory of the verification was based on observations without spatial resolution and the QPP loop geometry was unknown. For this kind of mechanism, another scenario proposes that the QPP emission follows from periodically distributed in space plasmoids, generated by a tearing instability in the flare current sheet, and following coalescence (Kliem, Karlický, and Benz, 2000). The individual bursts should appear at different spatial locations, gradually progressing along the arcade. The hard X-ray data show that the position of footpoint-like paired sources of individual bursts moved along the arcade (e.g. Grigis and Benz, 2005; Nakariakov and Zimovets, 2011; Gruszecki and Nakariakov, 2011; Inglis and Gilbert, 2013; Yang et al., 2009). The individual pulsations are emitted from footpoints of different magnetic loops. Acceleration (or injection) of the non-thermal electrons apparently occurred near the tops of those loops.

To identify the mechanisms of the QPPs we need knowledge of the geometry of the flare loops, the values of magnetic field, plasma density, and temperature. X-ray and microwave observations complement each other, since the mechanisms and conditions for the generation of radiation are essentially different. The HXR emission is emitted from electrons with energy up to a few hundred keV, while the microwave emission is generated by higher energy electrons. The radio spectra are dependent on magnetic-field properties in the QPP sources.

A number of events in which the quasi-periodic pulsations have been seen simultaneously in microwaves and hard X-rays have been studied (e.g. Nakajima et al., 1983; Aschwanden, 1987; Altyntsev, Grechnev and Hanaoka, 1998; Asai et al., 2001; Grechnev, White, and Kundu, 2003; Mészárosová et al., 2006). Similarity of light curves confirms a common origin for the electrons radiating in these electromagnetic emissions. The spatial resolved microwave data provide important additional information not only by spectral and spatial properties of the QPP events but also about the magnetic-field in the QPP sources.

Detailed studies of individual flares, which usually reveal peculiarities of specific flares, are essential for better understanding of the flare phenomena. In this article, we carried out detailed analysis of multi-wavelength observations of a limb flare on 18 August 2012. We analyzed the QPPs using a broad data set including high temporal, spectral, and spatial resolution X-ray, and microwave observations. The microwave emission of the flare was recorded by new spectropolarimeters and with the prototype of multiwave radioheliograph developed by the Siberian Solar Radio Telescope team. Also we used data recorded with the Wind/Konus (hereafter WK) γ -ray spectrometer onboard the Global Geospace Science Wind spacecraft. The instruments and observations are described in Section 2, the data are analyzed and discussed in Section 3, and the conclusions are drawn in Section 4.

2. Observations

A GOES M1.8 flare on 18 August 2012 occurred in the region NOAA 11548 (N19E86). From soft X-ray measurements with the GOES-15 spacecraft this flare started around 03:19 UT and achieved its maximum at 03:23 UT. The flare was well observed by the Siberian Solar Radio Telescope (SSRT), Ten-antenna prototype of the multifrequency Siberian radioheliograph, Nobeyama Radioheliograph (NoRH), Ramaty High Energy Solar Spectroscopic Imager (RHESSI) telescope, and the Atmospheric Imaging Assembly (AIA: Lemen et al., 2012) onboard the Solar Dynamics Observatory (SDO). In addition, we used records

of the total solar flux observed by the Solar Radio Spectropolarimeters (SRS), Badary Broadband Microwave Spectropolarimeter (BBMS), and Nobeyama Radio Polarimeter (NoRP). To study its temporal behavior in hard X-rays we included observations from RHESSI and the Wind/Konus, a γ -ray spectrometer.

2.1. Instrumentation

The microwave data with spatial resolution at 5.7 GHz were acquired with the SSRT (Grechnev et~al., 2003; Kochanov, Anfinogentov, and Prosovetsky, 2013). The SSRT is a cross-shaped interferometer producing two-dimensional full-disk images every three to five minites. At the flare time, the half widths of the SSRT beam was 19.6×20.3 arcsec. Using data from the 10-antenna prototype we have also studied locations and sizes of microwave sources at five frequencies (4.2, 4.9, 5.8, 6.9, and 7.4 GHz) with a cadence a 1.6 seconds (Lesovoi et~al., 2012). The estimates of the positions and sizes were made under the assumption of azimuthally symmetrical sources.

The flare was also observed by the NoRH, which has provided images of the solar disk at 17 and 34 GHz with a cadence as rapid as 0.1 seconds (Nakajima et al., 1994). A time series of maps were created using the Koshix software package (Hanaoka et al., 1994). During the present event the angular resolution was 12.3×12.8 arcsec and 8.1×8.3 arcsec at 17 and 34 GHz, respectively.

In our study we used the HXR data obtained with RHESSI (Lin *et al.*, 2002) in the energy band 3–300 keV. We used the forward-fit (FWD) method and the OSPEX algorithm for imaging and spectra fitting respectively. The FWD approach is rather effective for sources with a relatively simple structure such as the one we study here. Structure of the flare region was obtained with AIA.

We analyzed the dynamics of microwave spectrum and spatial characteristics of the QPP sources, using the new complex of spectral instruments. The BBMS provides fine spectral measurements of the total solar emission (Stokes parameters I and V) in the 4–8 GHz band with a temporal resolution of 10 ms (Zhdanov and Zandanov, 2011). For spectrum measurements we use data from the SRS spectropolarimeter (I and V fluxes at 16 frequencies: 2.3, 2.6, 2.8, 3.2, 3.6, 4.2, 4.8, 5.6, 6.6, 7.8, 8.7, 10.1, 13.2, 15.7, 19.9, 22.9 GHz; the temporal resolution was 1.6 seconds).

The microwave flare spectra were also recorded with the Nobeyama Radio Polarimeters (Shibasaki, Ishiguro, and Enome, 1979; Nakajima *et al.*, 1985). The NoRP has recorded total fluxes in intensity and polarization at 1, 2, 3.75, 9.4, 17, 35, and 80 GHz with a temporal resolution of 0.1 seconds.

To study hard X-ray temporal behavior, we have also used the Wind/Konus data. In the waiting mode WK records a time history in three energy ranges, G1, G2, G3, with bounds 21–81 keV, 81–324 keV, and 324–1225 keV, with a temporal resolution of 2.944 second. In the triggered mode, time history is measured in the same three channels with a resolution varying from 2 to 256 ms and a total record duration of 230 s, and also 64 spectra are measured in the 20 keV–15 MeV band. A detailed description of the experiment can be found in Aptekar *et al.* (1995), and a brief overview of solar flare observations with WK is given in Palshin *et al.* (2014). In our study we have used the 256 ms records in the G1, G2 ranges; the signal in the G3 range was too weak for this flare.

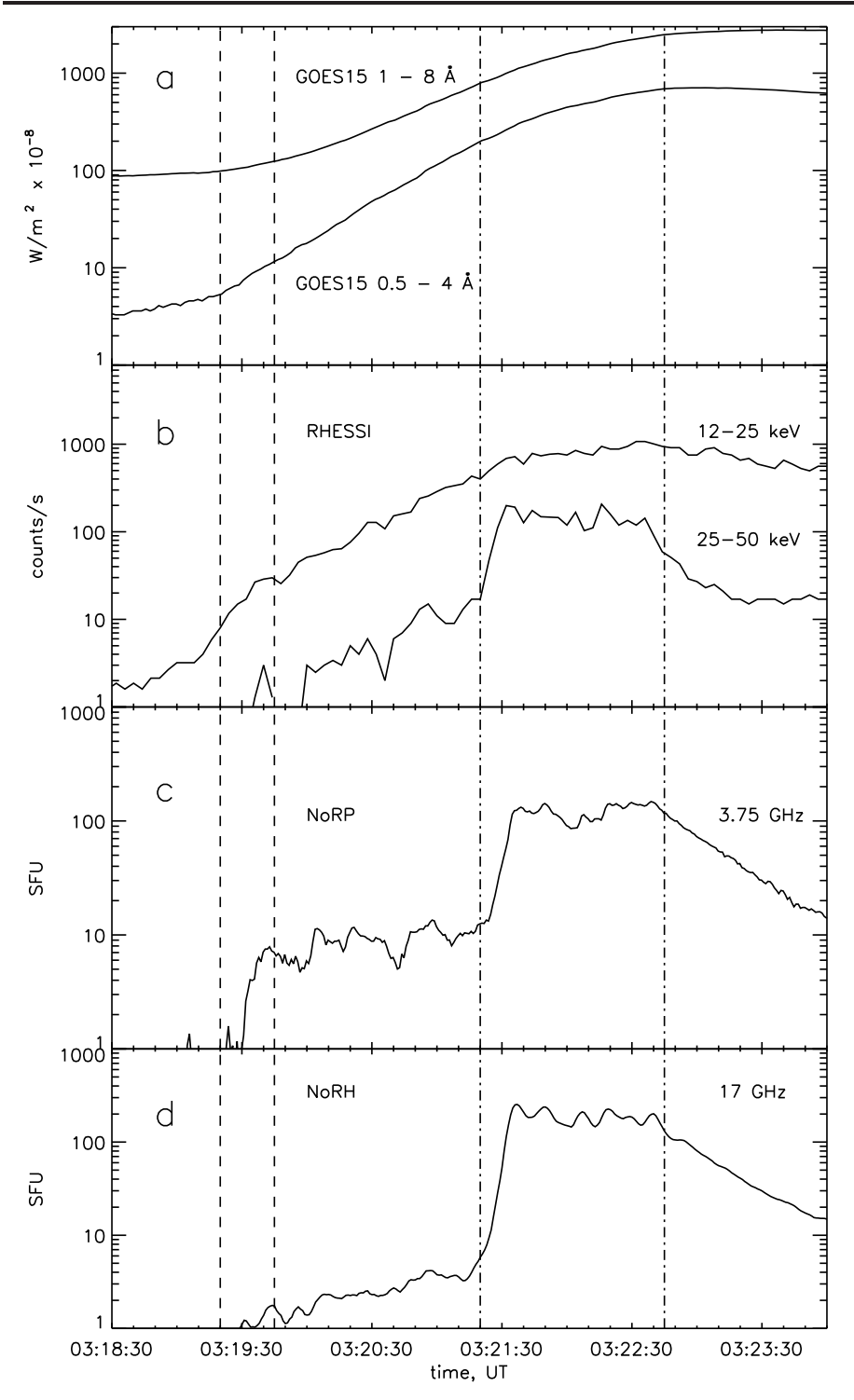


Figure 1. Soft (a) and hard (b) X-ray profiles together with microwave (c,d) fluxes. Dashed-vertical lines indicate interval with the fine spectral structures (see Figure 2), dash—dotted lines - interval with the QPPs (Figure 3).

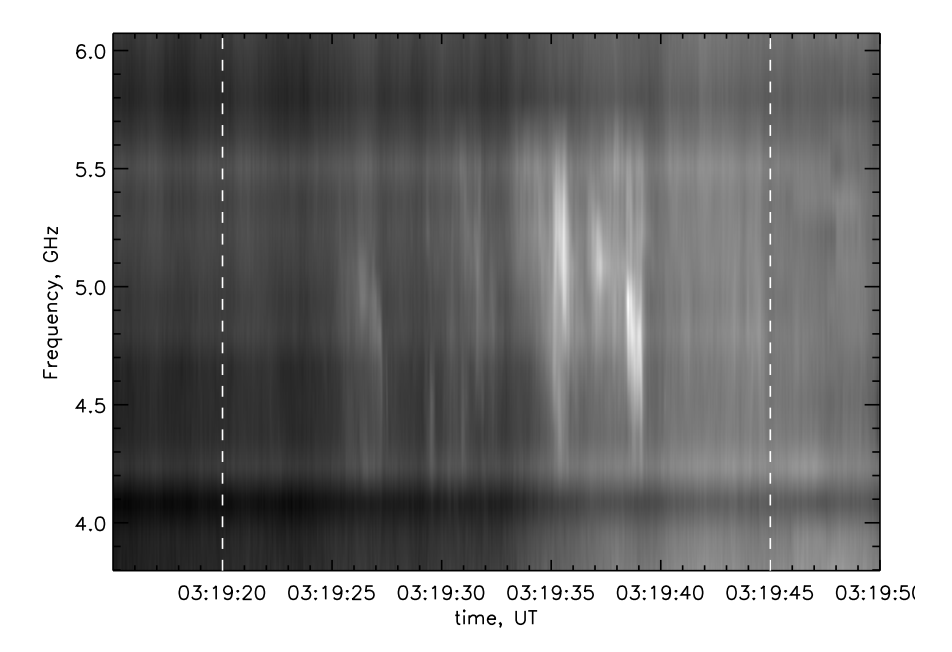


Figure 2. Portion of the dynamic spectrum, recorded with BBMS and dashed-vertical lines indicate interval with the fine spectral structure in Figure 1.

2.2. Total Flux Profiles

Light curves recorded during the flare in X-rays and microwaves are presented in Figure 1. The flare started in the soft X-rays at 03:19 UT and the GOES signals increased gradually during four minutes (panel a). Similar behavior was seen in the hard X-rays at energies below 25 keV (panel b). Clusters of frequency drifting subsecond structures (see Figure 2) appeared at the beginning of the flare at frequencies about 5 GHz. After that hard X-ray and microwave emission (b, c) began to rise.

After flare emission sharply increased around 03:21:24 UT, a series of QPPs occurred after that time in higher-energy X-ray channels and microwave frequencies. During an interval of one minute six prominent quasi-periodic pulses were recorded in hard X-rays and in microwaves (d). Note there was no apparent response in the GOES signals and low energy RHESSI channel. This shows that QPPs are related to non-thermal electrons.

The extended interval with the QPPs is presented in Figure 3. The first four panels show the microwave profiles measured by the SRS and NoRP/NoRH. The accuracy of microwave measurements can roughly be seen with the minor difference between the independently measured profiles shown by solid and dotted curves in the first three panels in Figure 3. In the course of the QPP stage there were two flux enhancements at 3.75 GHz (Figure 3,b) with duration about 30 seconds. The intervals with the enhancements are separated by the dotted line. The QPP modulation was more pronounced at high frequencies. The polarization

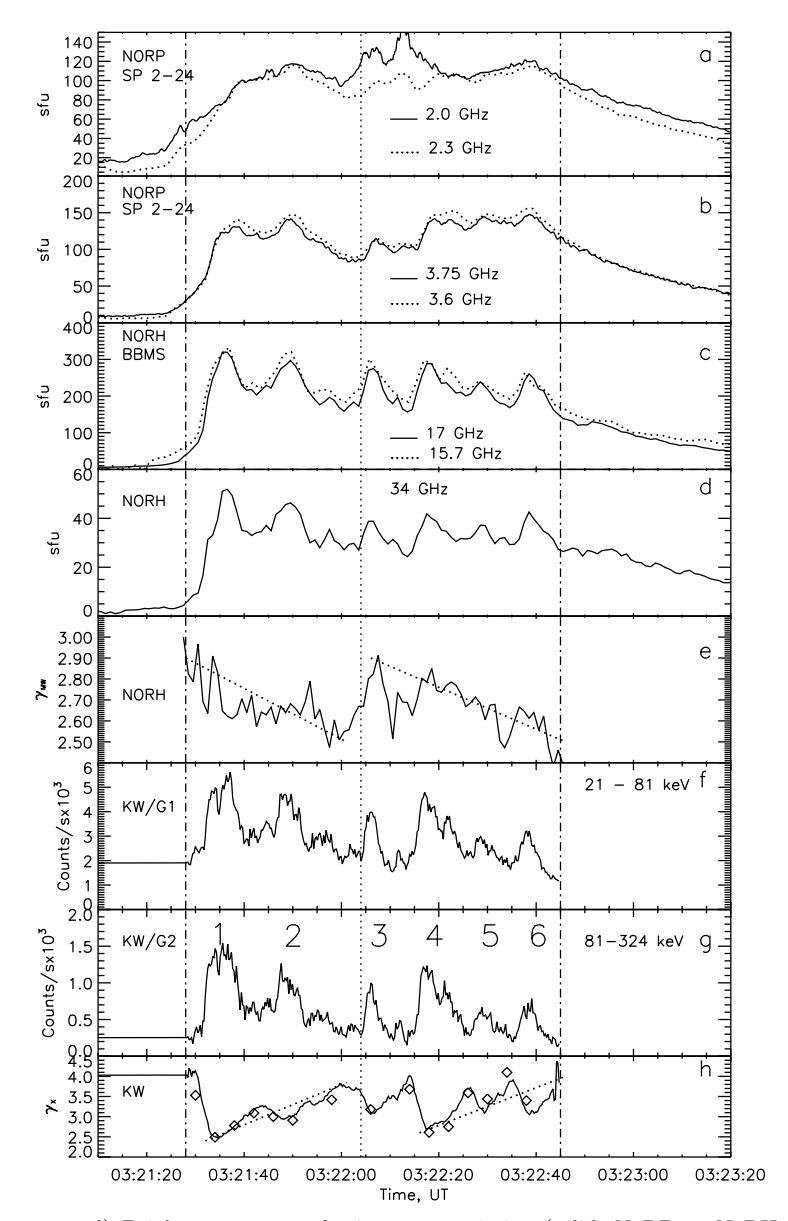


Figure 3. a-d) Brightness curves of microwave emission (solid: NoRP or NoRH, dotted: SRS) and hard X-rays (WK); e) Power-law index calculated from the ratio of 17 GHz and 34 GHz fluxes; f,g) Brightness curves of the HXR emission (WK); h) Power-law indices of the hard X-ray spectra measured with the RHESSI (rhombus). Solid curve shows the natural logarithm of the WK hardness ratio, G1/G2, multiplied by two. Vertical dash-dotted lines mark the bounds of the QPP interval and the dotted line shows the beginning of the second enhancement. The prominent pulses are numbered in the panel g. The inclined dotted lines (e,h) show index trends for each enhancement.

profiles are not shown because the polarization degrees did not exceed 0.05. The microwave spectrum slope $\gamma_{\rm MW}=\ln(F_{17}/F_{34})/\ln 2$, determined by the ratio of fluxes at 17 and 34 GHz, is shown in Figure 3e. Again we can see the two distinct intervals in behavior of $\gamma_{\rm MW}$ corresponding to the flux enhancements at the lower frequencies. During each interval the index was gradually decreasing from $\gamma_{\rm MW}=2.9$ to 2.5 with a timescale of 60-70 seconds. Hereafter, we will refer to these two intervals as the enhancements.

The hard X-ray profiles (G1, G2) measured with the Wind/Konus are shown in the panels (Figure 3, f, g). The signal in the G3 range was too weak to allow a meaningful analysis. Similar to MW emissions, the WK light curve shows two sets of decreasing QPPs. Note that the strongest X-ray pulses (No. 1,2,4) have a double/triple structure. The last panel (Figure 3h) presents the power law index of the hard X-ray spectrum measured with the RHESSI. The solid curve shows the natural logarithm of the WK hardness ratio (derived as the ratio of background-subtracted counts in the G1 and G2 ranges) multiplied by two. There is a good agreement between the temporal evolution of the index obtained from the fitting of the RHESSI spectra and the index obtained from the WK hardness ratio.

The trends of the power-law indexes γ_X during the enhancements (the dotted lines) showed the spectrum softening with the exponential growth time scale of 60 and 70 seconds, just opposite to the trend direction of the microwave index γ_{MW} The maxima of the QPP pulses corresponded to the local γ_X minima.

2.3. Flare Configuration

The flare occurred in a rapidly time-varying complex of large and small EUV loops over the eastern limb (Figure 4). The EUV images observed at the different emission lines show a filament eruption from the flare region which began around 03:21:15 UT. After that the microwave flux increased sharply at 03:21:24 UT. For X-ray and microwave emissions, two kind of sources can be seen. One belongs to an apparent footpoint source as observed at 17 GHz (including the polarization emission at 17 GHz) and higher-energies in X-ray such as \geq 25 keV, while another belong to a coronal source as observed at 5.7 GHz and lower energies in X-ray. The microwave coronal source seen at 5.7 GHz is located at a height of 20 arcsec above the limb. The fine spectral structures were emitted from the region pink crosses inside the central part of the 5.7 GHz source.

The SDO/AIA 211 Å image shows that 5.7 and 17 GHz sources were located in different loops. This image was created using the Interactive Data Language (IDL) shade surf procedure where the z-axis (not displayed here) means the 211 Å emission intensity in a log10 scale. It is seen that the 17 GHz sources in polarization corresponds to footpoints of the UV loop, having a height of 12 arcsec. It is worth noting that the coronal source, as seen both in microwave and X-ray, is co-spatial with the south leg of a larger loop (closely spaced loops system).

The relative brightness of sources at 17 GHz, where QPPs originate, changes considerably. The north footpoint is strengthening (right panel). Also the 34 GHz source appeared at this footpoint. After correction for the beam width the source

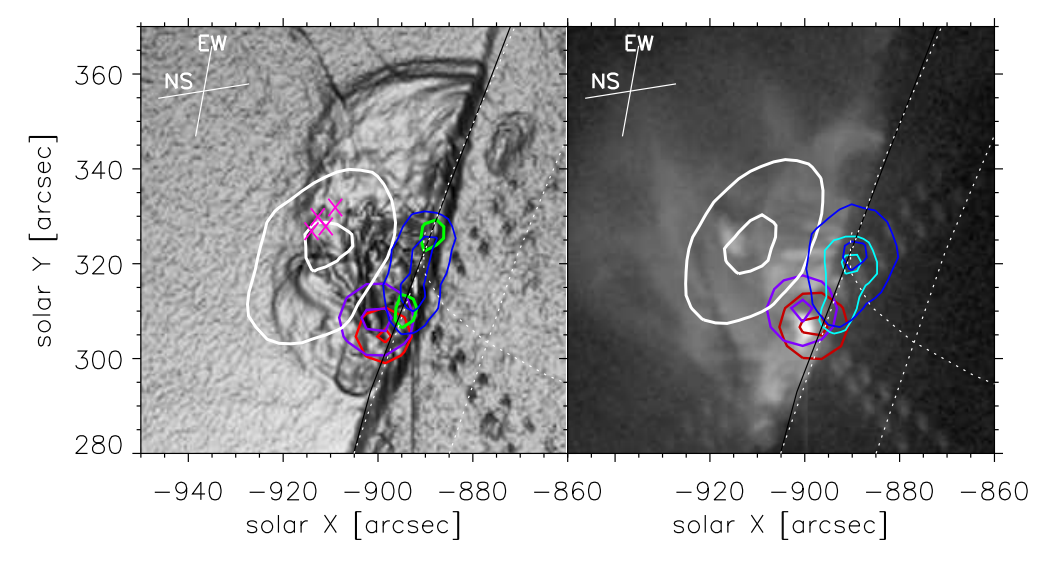


Figure 4. Flare structure before (left) and during (right) the QPPs appearance. Background - EUV images at 211/94 Å (03:21:11/03:21:27 in the left/right panel, respectively). White contours show continuum 5.7 GHz source (03:19/03:23, Stokes I). Blue contours – continuum 17 GHz source (Stokes I, 03:21:13/03:21:25); violet contours - 12–25 keV X-ray sources (03:21:15/03:21:37); red contours - 25–50 keV X-ray sources (03:21:15/03:21:37). Levels of contours are 50 % and 90 %. In the left panel the green contours shows the 17 GHz sources of polarized emission at 90 % level; pink crosses demonstrate source positions of the subsecond fine spectral emissions shown in Figure 2. In the right panel cyan contours present the 34 GHz source at 03:21:25. The axes show are seconds from the solar disk center. In the top left corner, the cross shows the scan directions of the SSRT linear interferometers; length of each line is the half width of the SSRT beam.

sizes at 17 and 34 GHz were close to each other and vary between 6-9 arcsec during the QPP interval. We have not found a relation between the QPPs and the size variations. The structure of the X-ray sources did not change during the QPP stage.

The apparent sizes of the SXR sources obtained by forward-fit algorithm are 10-15 arcsec. This is about twice as large as the bright patch at the same site seen in the SDO/AIA 94 Å image. The spatial resolution of the EUV images is high and it is reasonable to assume that the bright patch with size about 10 arcsec provided the main contribution to the soft X-ray emission. From the GOES-15 signals it follows that emission measure is 2.7×10^{48} cm⁻³ and temperature is 16-18 MK during the QPP stage. We used the standard SolarSoft procedure to compute the emission measure and temperature from the GOES data. The RHESSI spectrum fitting reveals the parameters $(0.8-2.2) \times 10^{48}$ cm⁻³ and 20-22 MK. Assuming that the source is a sphere of diameter 10 arcsec, we can estimate plasma density in X-ray source as $(0.7-1.2) \times 10^{11}$ cm⁻³. From the GOES measurement this parameter is roughly two times larger.

For the single 5.7 GHz sources, it was possible to study their spatial dynamics at a number of frequencies using the Ten-antenna interferometer observations. For a circular bright source the accuracy of the size and displacement measure-

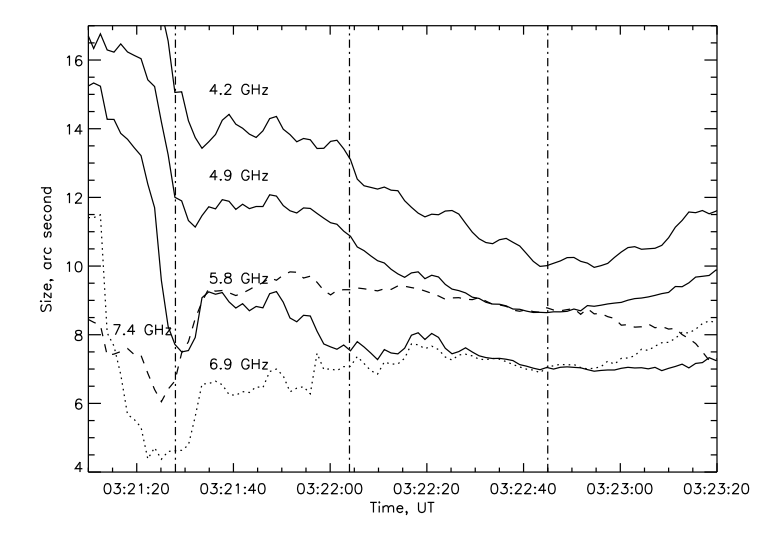


Figure 5. Size variations of the microwave source observed by the Ten-antenna prototype in the frequency range 4.2-7.4 GHz. Dash-dotted lines mark the interval with the QPPs.

ments is a few arcsec. Observations show that the size behavior depends on time and frequency (Figure 5). At 4.2–5.8 GHz the FWHM angular size of the coronal source decreases down to 8–14 arcsec during the first enhancement of the QPP stage. This process might belong to the phenomenon of contraction of flaring loops (Ji et al., 2006; Ji, Huang, Wang, 2007). The relation between the contraction and following oscillations appeared both in coronal loops and X-ray/microwave emission was studied in detail by Simoes et al. (2013). They interpreted the phenomena as persistent, semi-regular compressions of the flaring core region, which modulate the plasma temperature and emission measure. For the size of 4.2 GHz source, we can see an apparent oscillations, although there are no correlation between the size variations and QPP profiles at this resolution level. It is also worth noting that, at higher frequencies (6.9–7.4 GHz), the sizes are smaller and do not change significantly with time.

2.4. The QPP Properties

In order to characterize the QPPs at different waves we calculate the modulation amplitude for each time profile as mod_{ν} , which is the normalized modulation of the signal. The formula is given as follows, where t is the time in seconds, T_{QPP} =77 seconds is the duration of the QPPs interval, and F_{ν} is the flux density at a given frequency:

$$\operatorname{mod}_{\nu} = \left(\frac{1}{T_{\text{QPP}}} \int_{0}^{T_{\text{QPP}}} S_{\nu}^{2}(t) dt\right)^{1/2}, \text{ where } S_{\nu}(t) = \frac{F_{\nu} - \langle F_{\nu}(t) \rangle}{\langle F_{\nu}(t) \rangle}. \tag{1}$$

Table 1. Results of cross-correlation and modulation amplitude.

	mod	$K_{ m corr}$	τ , [s]
21-81 keV	0.26	0.95	< 0.3
$81-324~\mathrm{keV}$	0.35	1.00	0
$5.7~\mathrm{GHz}$	0.16	0.48	1.6
$9.4~\mathrm{GHz}$	0.16	0.61	1.3
$17~\mathrm{GHz}$	0.22	0.77	1.0
$34~\mathrm{GHz}$	0.27	0.69	0.5

Using the time profile of $81-324\,\mathrm{keV}$ as a reference, we carried out its cross-correlation with the time profiles of $21-81\,\mathrm{keV}$ and MW at 5.7, 9.4, 17, and 34 GHz. We obtained correlation coefficients $[K_{\mathrm{corr}}]$ and time delays $[\tau]$; all results including the modulation amplitude mod are given in Table 1. In this study we used the NORP records with 0.1 s resolution. Roughly, it can be considered that the signals in Table 1 ranged according the energy of emitting electrons, since the radio frequencies/X-ray energies are rather proportional to electron energy. It is clear that the modulation amplitudes decreased with decrease of the energy of electrons producing the X-rays and radio emission. Note that there was almost no time delay between the WK signals. From the sufficiently high correlation of the microwave emission with the X-ray pulses it follows that the upper microwave sources seen at 5.7 GHz are physically associated with the X-ray sources.

To find the QPP periods, we have performed the Fourier analysis of the X-ray and microwave profiles during the QPP interval. Figure 6 shows the normalized power spectra for the hard X-rays at $81-324\,\mathrm{keV}$, 17 GHz emission (from the north footpoint of the low loop), and 3.75 GHz emission (from the large loop source). All of these sources were oscillating with the common prominent period of 11 ± 1 second. In microwaves there were additional significant modes (above 0.5 level) with periods of 8 and 15 seconds, as well as some subsidiary peaks. The modes with periods of 8 seconds and 15 seconds corresponded to beat frequencies that were produced by oscillations with periods of 10.5 seconds and 33 seconds. The last period is close to the duration of the enhancements described above.

The cross-correlation coefficients $[K_{\rm corr}]$ were high for $21-81~{\rm keV}$ and $17~{\rm GHz}$ profiles. This confirmed that these sources were related to the same loop structure. The delay of microwave pulses originated from the conjugate footpoint of the low loop was about 1 second. The 5.7 GHz emission was delayed 1.6 seconds and value of $[K_{\rm corr}]$ was lower than at 17 GHz. This is consistent with the assumption of their localization in different magnetic loops.

The X-ray sources at different energies were located close to each other and it is acceptable to describe the spectral index behavior by the ratio of the signals recorded with different energy channels. It is seen in Figure 7 that the X-ray index changed in accordance with the emission amplitude variations. During every pulse the logarithmic value of signal in the energy channel of $81-324\,\mathrm{keV}$

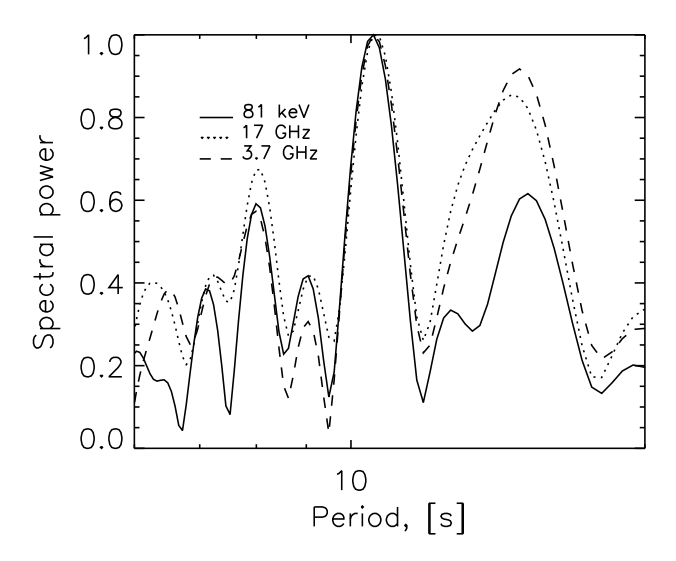


Figure 6. Normalized power spectra of emission at different waves: Wind/Konus detector in the range 81–324 keV, NoRP fluxes at 17 and 3.75 GHz. The squared magnitude of the discrete Fourier transform (power spectrum) are normalized and presented in periods.

depended linearly on the logarithmic ratio of 21-81 and $81-324\,\mathrm{keV}$ signals in both rise and fall phases (Figure 7). The observed soft-hard-soft evolution of the spectral features indicates that the every pulse can be considered as a primary energy release event.

The microwave spectrum at 03:21:37 UT (the peak of the first pulse) is shown in Figure 8. The spatial observations showed that this spectrum was mainly generated by two different sources: the upper source seen at 5.7 GHz and the near-limb source seen at 17 GHz. At high frequencies the spectrum was produced by the footpoint source with a size of 6-9 arcseconds. Therefore we assume that the spectral slope in the optically thin regime was directly related to the power law index of electrons in the north limb source. We have no reliable data on the low frequency spectrum slope of this limb source, but it should fall off sharply because the sources at 5.7 GHz and 17 GHz did not overlap in the radio maps.

The low-frequency part of the spectrum was emitted from the extended area of the large loops. The flat slope of the spectrum at frequencies below 10 GHz can be explained by the emission area increasing toward low frequencies (see Figure 5). Using the Ten-antenna prototype observations, we can estimate the spectrum emitted from the area of the 7.4 GHz source. To find the corresponding fluxes at 6.9, 5.8, 4.9, and 4.2 GHz, we have multiplied the observed fluxes by the factor of $(6/D)^2$, where [d] was the size at the given frequency in arcseconds, six arcseconds was the source size at a frequency of 7.4 GHz. The recalculated flux values are shown by crosses in Figure 8. The necessity of taking the changing size into account to interpret the low-frequency part of a spectrum has been

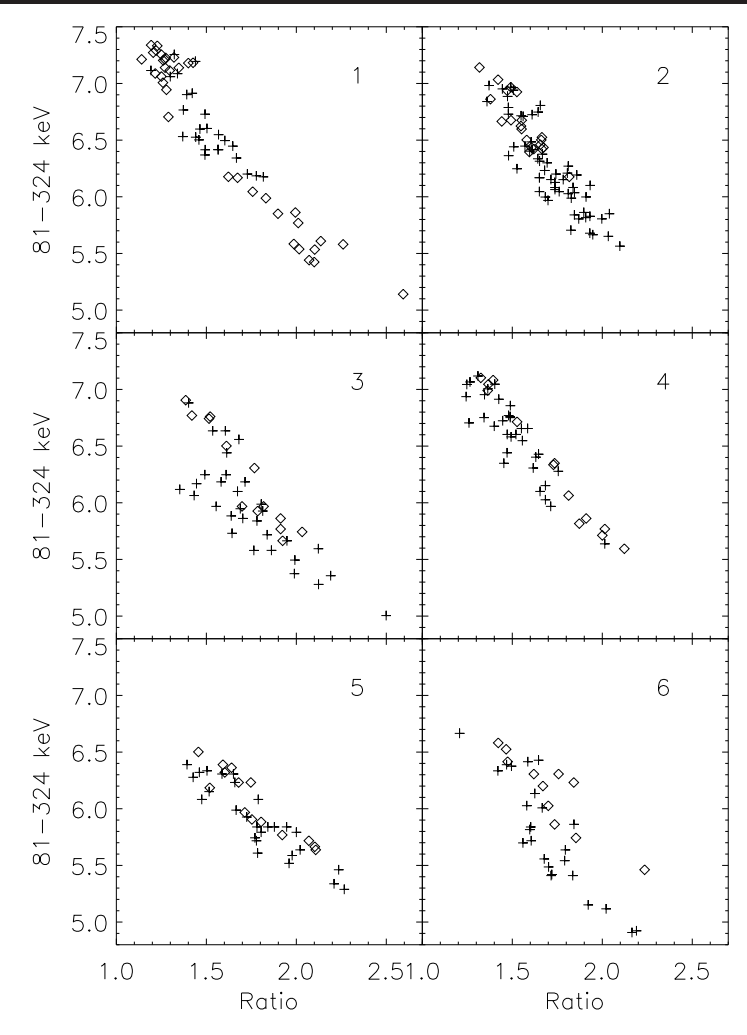


Figure 7. Soft-hard-soft behavior during the individual QPPs. The panels show the logarithmic dependences of G2 signals on the logarithms of the G1/G2 signal ratio for individual pulses marked by numbers in Figure 3g. Diamonds correspond to the rise phase of the pulse and crosses to the fall off.

emphasized by a number of articles (see, for example, the review by Bastian, Benz, and Gary (1998), Kundu *et al.* (2009) and Lee, Gary, and Zirin (1994)).

Key results of observations can be summarized as:

i) The X-ray emission at all observed energies was produced over the flare at the place where the south legs of the small and large loops were close to each other. The quasi-periodic pulses were observed in this source at photon energies above 25 keV. The QPP source seen at 17 and 34 GHz was located at the north conjugate footpoint of the low loops. Below 10 GHz, the continuum emission, subsecond, and quasi-periodic pulses originated from the high flare loops.

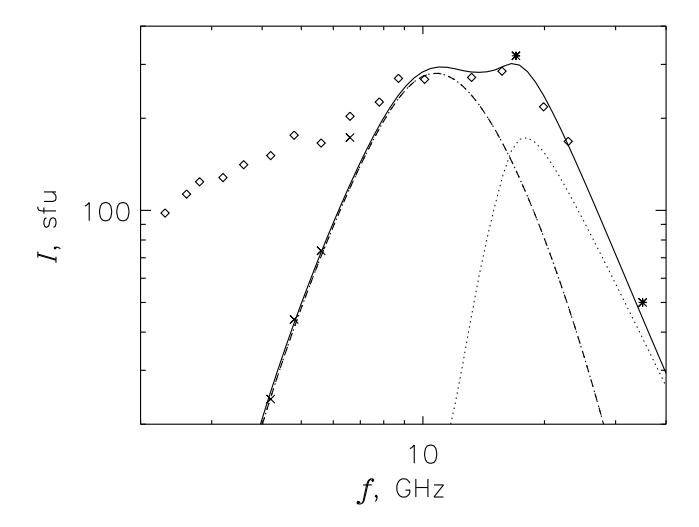


Figure 8. The MW spectrum during the peak of the first pulse (03:21:37) recorded by SRS (diamonds) and NoRH (asterisks). The normalized fluxes on the size of the source at 7.4 GHz are shown with crosses. The solid line indicates the result of spectrum fitting by two sources (dashed–dotted line: upper source and dotted line: near-limb source).

- ii) During the flare, the X-rays were characterized by thermal emission at energies below 25 keV. The emission measure and temperature were gradually increasing during the flare. In microwaves the signatures of the non-thermal electrons appeared after the flare onset.
- iii) The sharp growth of nonthermal electron population began several seconds after the filament eruption from the flare region. During the one-minute interval the microwave and hard X-ray emissions displayed the QPPs that were repeated in a period of 10.5 seconds and highly correlated with each other. The background of QPPs consisted of two successive intensity enhancements of 30-40 seconds durations with sharp rise edges and slowly decaying tails.
- iv) The microwave QPPs were delayed relative to the hard X-ray emission. The delays of the low frequency pulses were up to 1.8 seconds at the upper source. At the limb source, the delays of the high-frequency ones were a factor of two smaller.
- v) During the QPPs there were the linear relationships between logarithms of X-ray flux magnitude and the power-law index. At long times there were different behaviors of the microwave and X-ray emissions. The power law index of the HXR emission became gradually softer during the enhancements, but the microwave-spectrum slope became harder in that time.

3. Data Interpretation

3.1. Flare Configuration

To identify the QPP mechanism, we must determine the configuration of the flare loops and their plasma parameters. At first glance the locations of the flare sources (two high-frequency sources near the limb and one well above them) point to the so-called standard solar-flare model (CSHKP model). Furthermore, the flare was associated with the filament eruption. However, in the event under study, there were no motions of the sources and the light curves at footpoints were not delayed relative the top source. Thus, for the studied flare we could assume two possible scenarios: i) with the reconnection at space under rising eruptive filament (Forbes, 2000), and ii) with the reconnection between interacting flare loops (Hanaoka, 1996). In the first scenario the upward motion of the filament should be seen in the 5.7 GHz images (Uralov et al., 2002). However, no such a motion was observed.

Although the standard flare scenario cannot be excluded, in the following interpretation of the X-ray and radio sources we assumed the scenario with the interacting loops and made the estimations of plasma parameters described in detail below. The flares in a configuration of two interacting current-carrying loops were firstly described by Hanaoka, 1996. A number of flares was found to fit such quadrupolar geometry (see also Hanaoka, 1997; Nishio et al., 1997; Aschwanden et al., 1999). The energy-release interaction happens between the small flare loops system and large loops with footpoints close to each other (see cartoons in the articles cited above).

The sharp growth of energy release during the QPP stage can be excited by magnetic structure disturbances caused by the filament eruption from the flare region. The QPP similarity in X-rays and microwaves means that high-energy electrons are produced at the energy release site and propagate over to the remote sites. Although the temporal modulation of the radio flux closely mimiked the hard X-ray pulses, the radio profiles were delayed by 0.5-1 seconds and 1.8 seconds. The 17 GHz emission is generated by relativistic electrons and the transit time of 20 arcseconds does not exceed 50 ms. The delays between the emissions from an energy release site and some remote place can be increased due to large pitch-angles of accelerated electrons. To provide the delay of 1 second the pitchangle must be in unrealistic bounds of a few degrees. The delays of such duration can be explained by energy dependent trapping of emitting electrons. Note that for a one-loop configuration there should be a progressive delay of peaks emitting by higher-energy electrons due to the effect of Coulomb collisions on the trapped electrons (Bai, 1982). In our case the tendency was the opposite and the delays were shorter at high frequencies. In the event under study, the QPPs had the soft-hard-soft X-ray behavior and therefore the relatively large delays at low frequencies could not be explained by an energy dependent injection. So, all of these reasons confirm the suggestion about the two-loop configuration of the flare.

3.2. X-ray Source

The size of the X-ray source was about 7–10 arcseconds and did not exceed the free path of electrons with energies up to a few keV. In this source the plasma was heated a few minutes before the QPP stage. At this stage we estimated the temperature as $T=16-22\,\mathrm{MK}$ and plasma density $n=(1-2)\times10^{11}\,\mathrm{cm}^{-3}$. The hot plasma region was stable over the flare duration and thus we estimated the magnetic-field strength in this source from the pressure balance as $B\geq\sqrt{16\pi\mathrm{k_BnT}}\approx100-170\,G$, where $\mathrm{k_B}$ is the Boltzmann constant.

On the other hand the magnetic value would not exceed this value considerably because the microwave emission from this source was weak. We have estimated radio emission of thermal electrons from the X-ray source site using the GX Simulator developed by Fleishman, Kuznetsov (2010). It strongly depends on the value of the magnetic field (see Altyntsev et al., 2012). Calculation showed that the 5.7 GHz flux should be above a detectable level of a few sfu for magnetic field above 200 G. So the magnetic field should not exceed this value and we shall use the value of 150 G in the following.

The QPP appearance corresponded to the sharp increase of the non-thermal electron population. Before the QPPs the X-ray power law index was about $\gamma=4.1$, and at the first pulse γ decreased to 2.5. The QPP stage consisted of the two X-ray enhancements of approximately equal durations of about 30 seconds. Each enhancement started rising sharply and then the background intensity was decreasing gradually. The X-ray hardness of background emission was varying during these intervals from 2.5 to 3.7 with a timescale of 60-70 seconds (Figure 3h).

The durations of rise and decay phase of the individual pulses were the same. The X-ray signals during the pulses were varying in accordance with the spectral index changing, i.e. the index had a soft-hard-soft behavior (Figure 7). Thus the trapping of the non-thermal electrons was weak in the interaction region.

3.3. The Microwave Sources

The spatially unresolved spectrum of microwave emission at the first MW peak (03:21:37 UT) is shown in Figure 8. From the radio maps it follows that the spectrum consists of two main components emitted by the upper and limb sources at low and high frequencies, respectively. Firstly we consider the limb source producing the high-frequency slope of the spectrum.

The high-frequency source was seen at 17 and 34 GHz with the sizes close to the NoRH beam widths. For spectrum modeling that we used, the source size of 8 arcseconds and the fluxes recorded at 17, 19.9, 22.9 GHz with the SRS and NoRH. The viewing angle 85 degrees was taken from the flare-site longitude. We can not determine the low-frequency part of the spectrum, but it must have rapidly decreased because this source was not seen in the 5.7 GHz images.

The dotted curve in Figure 8 presents the result of spectrum fitting of the high-frequency source for the isotropic distribution of emitting electrons. From calculations using the code of Fleishman, Kuznetsov (2010) it follows that the spectrum slope at frequencies above 20 GHz can be produced by the gyrosynchrotron emission of electrons with energy up to ≈ 0.8 MeV and power-law

index $\delta_{\rm MW}=3.55$. Note, the electron index $[\delta_{\rm MW}]$ was practically equal to the index $\gamma_{\rm X}=3.53$ of the X-ray flux from the energy release site. It is known that the flux index into the HXR target cannot be compared directly with the index determined from the microwave spectrum, since the radio emission is generated by the total number of radiating electrons in the coronal volume, rather than a flux. The measured value is in the bounds of the estimates $\delta_{\rm MW}=\gamma_{\rm X}+1.5$ and $\delta_{\rm MW}=\gamma_{\rm X}-0.5$ for the radio-emitting electrons depending upon whether we assume thick target or thin-target approximation for the X-ray source (e.g. White, Benz, and Christe, 2011).

To shift the spectrum turnover frequency up to 17 GHz and to suppress the emission at the lower frequencies, the magnetic field must be sufficiently large in the source. In this fitting the value of magnetic field is taken to be 950 G. Note that the Kosugi, Dennis, and Kai (1988) have found that the footpoint flare emission at 17 GHz is generated frequently by electrons with energy of a few hundreds of keV in layers with magnetic field 900–1000 G. So the difference in microwave emission from the low-loop footpoints can be explained by the large difference of their magnetic fields. The complementarities of asymmetric hard X-ray and radio emission have been verified in several observations (e.g. Wang et al., 1995).

During the enhancement, the average microwave index $[\gamma_{MW}]$ was slowly decreasing with exponential-decay time scale of 220-270 seconds. The corresponding trends are shown by the dotted lines. Hereafter, we will refer to these two intervals as the enhancements. It is remarkable that the long-term behavior of emission at 17 and 34 GHz has the opposite tendency from the X-rays. Consequently the acceleration process became weaker along the enhancements but the trapping provided the slowly hardening of radio emitting electrons.

For the limb source the microwave modulation levels were less than in the hard X-rays by a factor of 1.5 (Table 1). There was no clear response of the index MW of the individual pulses. Spectrum modeling showed that the observed modulation level of 0.25 can be achived when the varying of the power-law index of emitting electrons is below 0.05.

The low-frequency source was located well above the limb. Although the size of the source was changing with frequency it was possible to find the spectrum of a constant-size region using observations with the Ten-antenna prototype. The corrected spectrum is shown by crosses in Figure 8 for the central region of 6 arcseconds size. The dashed–dotted curve depicts the result of matching the low-frequency part of the spectrum by gyrosynchrotron radiation based on the following assumptions about parameters of non-thermal emitting electrons in the coronal source: the source area is taken to be equal to the area of a circle of six arcseconds in diameter; the magnetic-field vector direction to the line of sight is 85 degrees; the energy spectrum with an power-law index of 3.25.

The optically thick part of the gyrosynchrotron spectrum is determined by the density of emitting electrons and magnetic-field strength. In Figure 8 the spectrum model was obtained with a density of emitted electrons of 10^9 cm⁻³ with energy above 20 keV and magnetic-field strength $B{=}180$ G. The last value was close to the magnetic-field estimate in the loop-interaction region. The density of background plasma was 5×10^{10} cm⁻³. This density value is in accordance

with observations of the fine structures at frequencies about 6 GHz near the top of the high loop. It is known that at such frequencies the fine spectral structures are produced due to plasma mechanisms at a frequency about the harmonic of the local Langmuir frequency (Meshalkina et al., 2004). The modulation levels were less than in the hard X-rays and limb source (Table 1). Spectrum modeling showed that the modulation level of 0.16 can be achieved when the variation of the power-law index of emitting electrons is about 0.1.

3.4. The QPP Modulation

The source position was not changing during the QPP stage. Therefore we cannot interpret the QPPs using models in which the individual pulses correspond to different flare loops or spatially distributed plasmoids. Another peculiarity is the smooth behavior of the quasi-thermal emissions from the site coincided with the QPP source. So there are no clear modulation-induced heating effects.

The power spectrum revealed the main X-ray modulation mode with a period of 10.5 seconds (Figure 6), which has been excited twice during the QPP stage with interval of around 30 seconds. The microwave QPPs occurred with the same periodicity, but with the delays discussed above. So we consider that the pulsed acceleration, which occurred at a place close to the X-ray sources, was the driver of the broad-band emission pulses. During the every pulse, the hardness of the X-rays has a soft-hard-soft behavior with the index modulation of the order of a few tenths. Grigis and Benz (2006) and Fleishman, Toptygin (2013) showed that a similar soft-hard-soft trend is expected from a transit-time damping stochastic acceleration model that included escape of particles from the accelerator.

It is established that the QPPs can appear due to some intrinsic property of the energy-release process. The current-loop-coalescence instability proposed by Tajima, Brunel, and Sakai (1982) and Tajima et al. (1987) belongs to this category. The authors studied flares with the QPP time profiles and found that their properties can be explained by development of current-carrying-loops coalescence instability. They showed that the main characteristics of the fast or explosive reconnection can be summarized as follows: (i) large amount of impulsive increase in the energy of particles; (ii) appearance of quasi-periodic amplitude oscillations in nonthermal fluxes; (iii) double-peak (and triple-peak) structures in these oscillations. The multiple-peak behavior of the accelerated electrons is due to temporal variation of an electrostatic field in the coalescence process. All of these characteristics, including the subpeaks in the strongest hard X-ray pulses, were observed in the flare under study. The oscillation period in the hard X-ray or microwave emission should be about the Alfvén transit time "across" the interacting loops. To estimate this timescale we can take the values $n = (1-2) \times 10^{11} \text{ cm}^{-3}$ and size of ten arcseconds determined above. The Alfvén transit time across the energy release site is close to the QPP period of 10 seconds for reasonable value of magnetic field of 100-150 G. This estimate depends on the values of the density and the size of the source, which are not known accurately, and the quantitative estimates are coarse.

On the other hand, such periodic processes can interact with MHD oscillations of the loops and can be affected by them (e.g. review by Nakariakov and

Table 2. Physical values of flare loop

Loop	small	large
length [L:Mm]	17	70
temperature [T:MK]	20	20
density $[n, 10^{11} : cm^{-3}]$	1.5	0.5
magnetic field [B:G]	500	150
$\tau_{sausage}$ [s]	9.9	93
$ au_{kink}$ [s]	13/j	101/j
$ au_{slow}$ [s]	49	203
$\tau_{torsion}$ [s]	$13/\mathrm{m}$	$101/\mathrm{m}$

Melnikov, 2009). Using the source parameters for the loops determined above we can roughly estimate the oscillation periods (Table 2, where m is the number of windings along the loop for torsional mode, j-1 is the number of nodes for kink mode). The loop lengths are taken from the EUV image (Figure 4). To calculate periods we used formulaes (9-12) from Mossessian and Fleishman (2012). It is seen that the main observed period of 10 seconds can be excited in the small loop as sausage, kink, and torsional modes. In the large loops, such periods can be realized by the kink and torsion waves but for too high harmonic numbers.

The global sausage mode is a compressive mode with a wavelength of twice the loop length. Magnetic-field perturbations are maximum at the loop apex and minimum at the footpoints where the electron acceleration was modulated in the event under study. The mode is essentially compressible and there should be a modulation of the quasi-thermal X-ray emission from the loop body. Thus the observations do not support the sausage origin of the modulation. The kink and torsion modes are practically incompressible and more favorable.

The observed periodicity revealed one more timescale about 30 seconds. The flux oscillations at low frequencies with the same period were seen from the flare beginning and can relate to low harmonics of kink or torsion mode in the high loop. The kink oscillations should be seen due to the sources shifting in time. We have not observed source-position movement corresponding to the kink oscillations, but the spatial resolution of the measurements is probably not sufficient. The appearance of the pronounced QPP stage may be associated with the increase in the oscillation amplitude after the filament eruption.

4. Conclusion

The QPP observations in flares with the relatively weak trapping of accelerated particles provide a perspective to study primary-energy-release processes. In such events, these processes are well expressed, and periodicity properties provide supplementary keys for verification of interpretations.

We have made estimations of the periods of the measured pulsations taking the parameters from observations in the probable flare scenario of two-loop coalescence. The spatial observation showed that there were three QPP sources, whose positions were not changing before and during the QPP stage. Every pulse can be considered as an elementary acceleration event with soft-hard-soft behavior. The X-ray index changed in accordance with the emission-amplitude variations.

The spatial observations at different frequencies have showed that the low-frequency slope of the microwave spectrum can be explained by changing of the emission area. The characteristic timescales of the QPPs are in accordance with estimates of the Alfvén transit time across the interacting region. During the QPP stage the microwaves were generated by non-thermal electrons due to the gyrosynchrotron mechanism. The microwave pulses could be described as the response to the relatively small variations of the emitting electron hardness.

Acknowlegement

We thank the anonymous referee for valuable comments. We are grateful to the teams of the Siberian Solar Radio Telescope, Nobeyama Radio Observatory, and RHESSI, who have provided open access to their data. This study was supported by the Russian Foundation of Basic Research (15-02-01089, 15-02-03717, 14-02-91157), the Program of basic research of the RAS Presidium. The authors acknowledge the Marie Curie PIRSES-GA-2011-295272 RadioSun project. H. Mészárosová and M. Karlický acknowledge support by grants P209/12/0103 (GACR) and the research project RVO: 67985815 of the Astronomical Institute AS. The work is supported in part by the grants of Ministry of education and science of the Russian Federation (State Contracts 16.518.11.7065 and 02.740.11.0576). The Wind/Konus experiment is supported by a Russian Space Agency contract.

Disclosure of Potential Conflicts of Interest

The authors declare that they have no conflicts of interest.

References

Altyntsev, A.T., Grechnev, V.V., Hanaoka, Y.: 1998, Solar Phys. 178, 137. ADS. DOI.

Altyntsev, A.T., Fleishman, G.D., Lesovoi, S.V., Meshalkina, N.S.: 2012, Astrophys. J. 758, 138. ADS. DOI.

Aptekar, R.L., Frederiks, D.D., Golenetskii, S.V., Ilynskii, V.N., Mazets, E.P., Panov, V.N., Sokolova, Z.J., Terekhov, M.M., Sheshin, L.O., Cline, T.L., Stilwell, D.E.: 1995, Space Sci. Rev. 71(1–4), 265. ADS. DOI.

Asai A., Shimojo, M., Isobe, H., Morimoto, T., Yokoyama, T., Shibasaki, K., Nakajima, H.: 2001, Astrophys. J. 562, L103. ADS. DOI.

Aschwanden, M.J.: 1987, Solar Phys. 111, 113. ADS. DOI.

Aschwanden, M.J., Kosugi, T., Hanaoka, Y., Nishio, M., Melrose, D.B.; 1999, Astrophys. J. 526, 1026. ADS. DOI.

Bai, T.: 1982, Astrophys. J. 259, 341. ADS. DOI.

Bastian, T.S., Benz, A.O., Gary, D.E.: 1998, Astron. Astrophys. Rev. 36, 131. ADS. DOI.

```
Fleishman, G.D., Kuznetsov, A.A.: 2010, Astrophys. J. 721, 1127. ADS. DOI.
```

Fleishman, G.D., Toptygin, I.N.: 2013, Mon. Not. Roy. Astron. Soc. 429, 2515. ADS. DOI.

Forbes, T.G.: 2000, J. Geoph. Rev. 105, 23153. ADS. DOI.

Grechnev, V.V., White, S.M., Kundu, M.R.: 2003, Astrophys. J. 588, 1163. ADS. DOI.

Grechnev, V.V., Lesovoi, S.V., Smolkov, G.Ya., Krissinel, B.B., Zandanov, V.G., Altyntsev, A.T., Kardapolova, N.N., Sergeev, R.Y., Uralov, A.M., Maksimov, V.P., Lubyshev, B.I.: 2003, Solar Phys. 216, 239. ADS. DOI.

Grigis, P.C., Benz, A.O.: 2005, Astrophys. J. Lett. 625, L143. ADS. DOI.

Grigis, P.C., Benz, A.O.: 2006, Astron. Astrophys. 458, 641. ADS. DOI.

Gruszecki, M., Nakariakov, V.M.: 2011, Astron. Astrophys. 536, id.A68, 7. ADS. DOI.

Inglis, A.R., Gilbert, H.R.: 2013, Astrophys. J. 777, 30. ADS. DOI.

Hanaoka, Y., Shibasaki, K., Nishio, M., Enome, S., Nakajima, H., Takano, T., Torii, C., Sekiguchi, H., Bushimata, T., Kawashima, S., Shinohara, N., Irimajiri, Y., Koshiishi, H., Kosugi, T., Shiomi, Y., Sawa, M., Kai, K.: 1994, In: Proceedings of Kofu Symposium, Kofu, Japan, ed. by S. Enome and T. Hirayama, 35.

Hanaoka, Y.: 1996, Solar Phys. 165(2), 275. ADS. DOI.

Hanaoka Y.: 1997, Solar Phys. 173, 319. ADS. DOI.

Ji, H., Huang, G., Wang, H.: 2007, Astrophys. J. 660, 893. ADS. DOI.

Ji, H., Huang, G., Wang, H., Zhou, T., Li, Y., Zhang, Y., Song, M.: 2006, Astrophys. J. Lett. 636, L173. ADS. DOI.

Kallunki, J., Pohjolainen, S.: 2012, Solar Phys. 280(2), 491. ADS. DOI.

Kliem, B., Karlický, M., Benz, A.O.: 2000, Astron. Astrophys. 360, 715. DOI.

Kochanov, A.A.; Anfinogentov, S.A.; Prosovetsky, D.V.: 2013, Pub. Astron. Soc. Japan 65, No.SP1, Article No.S19. ADS. DOI.

Kosugi, T., Dennis, B., Kai, K.: 1988, Astrophys. J. 324, 1118. ADS 1988ApJ...324.1118K.

Kundu, M.R., Grechnev, V.V., White, S.M., Schmahl, E.J., Meshalkina, N.S., Kashapova, L.K.: 2009, Solar Phys. 260(1), 135. ADS. DOI.

Lee, J.W., Gary, D.E., Zirin H.: 1994, Solar Phys. 152, 409. ADS. DOI.

Lemen, J.R., Title, A.M., Akin, D.J., et al.: 2012, Solar Phys. 275, 17. ADS. DOI.

Lesovoi, S.V., Altyntsev, A.T., Ivanov, E.F., Gubin, A.V.: 2012, Solar Phys. 280(2), 651. ADS. DOI.

Lin, R.P., Dennis, B.R., Hurford, G.J., Smith, D.M., Zehnder, A., Harvey, P.R. and 57 coauthors: 2002, Solar Phys. 210, 3. ADS. DOI.

Meshalkina, N.S., Altyntsev, A.T., Sych, R.A., Chernov, G.P., Yan, Y.: 2004, Solar Phys. 221, 85. ADS. DOI.

Mossessian, G., Fleishman, G.D.: 2012, Astrophys. J. 748(2), 140. ADS. DOI.

Mészárosová, H., Karlický, M., Rybák, J., Fárník, F., Jiřička, K.: 2006, Astron. Astrophys. 460, 865. ADS. DOI.

Nakajima, H., Kosugi, T., Kai, K., Enome, S.: 1983, *Nature* 305, 292. ADS. DOI.

Nakajima, H., Sekiguchi, H., Sawa, M., Kai, K.; Kawashima, S.: 1985, Pub. Astron. Soc. Japan 37, 163, ADS.

Nakajima, H., Nishio, M., Enome, S., Shibasaki, K., Takano, T., Hanaoka, Y., Torii, C., Sekiguchi, H., Bushimata, T., Kawashima, S.: 1994, in Proc. IEEE 82(5), 705. ADS.

Nakariakov, V.M., Foullon, C., Verwichte, E., Young, N.P.: 2006, Astron. Astrophys. 452, 343.
ADS. DOI.

Nakariakov, V.M., Melnikov, V.F.: 2009, Space Science Reviews 149, 119. ADS. DOI.

Nakariakov, V.M., Zimovets, I.V.: 2011, Astrophys. J. Lett. 730, L27, 4. ADS. DOI.

Nishio, M., Yaji, K., Kosugi, T., Nakajima, H., Sakurai, T. et al.: 1997, Astrophys. J. 489, 976. ADS.

Palshin, V.D., Charikov, Yu.E., Aptekar, R.L., Golenetskii, S.V., Kokomov, A.A., Svinkin, D.S., Sokolova, Z.Ya., Ulanov, M.V., Frederiks, D.D., Tsvetkova, A.E.: 2014, Geomagnetism and Aeronomy, 54, 943. ADS. DOI.

Roberts, B., Edwin, P.M., Benz, A.O.: 1984, Astrophys. J. 279, 857. ADS. DOI.

Shibasaki, K., Ishiguro, M., Enome, S.: 1979, Nagoya University, Research Institute of Atmospherics, Proceedings, 26, 117. ADS.

Simoes, P.J.A., Fletcher, L., Hudson, H.S., Russel, A.J.B.: 2013, Astrophys. J. 777, 152. ADS. DOI.

Tajima, T., Brunel, F., Sakai, J., : 1982, Astrophys. J. Lett. 258, L45. ADS. DOI.

Tajima, T., Sakai, J., Nakajima, H., Kosugi, T., Brunel, F., Kundu, M.R.: 1987, Astrophys. J. 321, 1031. ADS. DOI.

- Uralov, A.M., Lesovoi, S.V., Zandanov, V.G., Grechnev, V.V.: 2002, Solar Phys. 208, 69. ADS. DOI.
- Wang, H., Gary, D.E., Zirin, H., Schwartz, R.A., Sakao, T., Kosugi, T., Shibata, K.: 1995, Astrophys. J. 453, 505. ADS. DOI.
- White, S.M.; Benz, A.O.; Christe, S.: 2011, Space Sci. Rev., 159, 225. ADS. DOI.
- Yang, Ya-Hui, Cheng, C.Z., Krucker, Sam, Lin, R.P., Ip, W.H.: 2009, $\ Astrophys.\ J.$ 693, 132. ADS. DOI.
- Zhdanov, D.A., Zandanov, V.G.: 2011, European Astrophys. Bul., 35, 223. ADS.